



# Photoreforming of plastic waste poly (ethylene terephthalate) via in-situ derived CN-CNTs-NiMo hybrids

Xueqin Gong<sup>a</sup>, Fengxia Tong<sup>a</sup>, Fahao Ma<sup>a</sup>, Yujia Zhang<sup>a</sup>, Peng Zhou<sup>a</sup>, Zeyan Wang<sup>a</sup>,  
Yuanyuan Liu<sup>a</sup>, Peng Wang<sup>a</sup>, Hefeng Cheng<sup>a</sup>, Ying Dai<sup>b</sup>, Zhaoke Zheng<sup>a,\*</sup>, Baibiao Huang<sup>a,\*</sup>

<sup>a</sup> State Key Laboratory of Crystal Materials, Shandong University, Jinan 250100, China

<sup>b</sup> School of Physics, Shandong University, Jinan 250100, China

## ARTICLE INFO

### Keywords:

Photoreforming of plastics  
In-situ derived CNTs  
Strong  $\pi$ - $\pi$  interaction  
Charge transfer  
Single-particle photoluminescence study  
Hydrogen evolution

## ABSTRACT

Photoreforming of plastic waste is a novel approach, which can not only degrade plastic waste into valuable chemicals, but also produce high-energy-density hydrogen fuels. Here, we developed an in-situ derived carbon nitride-carbon nanotubes-NiMo hybrids via NiMo-assisted catalysis route, which works as an efficient and stable photocatalyst for plastics photoreforming. The strong  $\pi$ - $\pi$  interaction between in-situ derived CNTs and CN promotes electron transfer, increases carrier lifetime and improves photocatalytic activity. The DFT calculations and single-particle PL quenching phenomenon confirmed the strong interface effect and charge transport for CN-CNTs-NM. In addition, the strong interaction between photocatalyst and ethylene glycol in plastics was observed in situ by single-particle PL. This work provides a smart strategy of utilizing in-situ derived  $\pi$ - $\pi$  interaction as well as direct evidence of the charge transfer from the photocatalysts to ethylene glycol, which provides guidance for the rational design of highly efficient photocatalysts for plastics photoreforming.

## 1. Introduction

Plastics are indispensable part of modern life and applied in various industries including food safety, medical health system and agriculture [1]. The global annual output of plastic products reached approximately 359 million tons [2]. As about 8 million tons of plastics entering the ocean, unrecyclable plastics present environmental problems and a huge loss of material value [3]. In particular, the production of poly (ethylene terephthalate) (PET) is ~30 million tons globally for in textiles and packaging (including bottles), but only 9% of PET is recycled [3]. A large amount of consumed plastics will cause "white pollution" because plastics are not degraded naturally. Polyethylene terephthalate (PET) plastic is a polyester made from terephthalic acid (TPA) and ethylene glycol (EG) monomers linked by ester bonds [4]. PET treatment can be divided into four main methods: landfill, incineration, chemical pyrolysis and regeneration granulation [5]. Nevertheless, high temperature or high pressure are necessary in most of strategies. To date, the development stable and high-performance catalysts to degrade plastics under milder conditions is highly desirable. Transforming plastic waste into valuable products and energy source is a major challenge to solve the global problem of plastic pollution.

Recently, photocatalytic technology has attracted extensive attention due to its cleanness and high efficiency [6,7]. Photoreforming of PET is one of the most promising technologies because it can harvest solar energy and convert it into hydrogen fuel with high energy density. H<sub>2</sub> is an ideal gas with high energy value and zero carbon emissions, which is a promising solution to the energy crisis [8,9]. To further improve the reactivity of plastics photoreforming, a pretreatment method is normally used to hydrolyze the plastics into monomeric ethylene glycol (EG) and other organic molecules in alkaline condition [10,11]. The organics such as EG from PET can not only works as electron donors, but also high value-added organic chemicals can be obtained. Recently, several photocatalysts have been reported to be applied for plastics photoreforming to produce hydrogen such as CdS/CdO<sub>x</sub> [10], CN/Ni<sub>2</sub>P [11] and TiO<sub>2</sub>/Pt [12]. To improve the performance of plastics photoreforming, it is important to develop a stable and efficient photocatalyst under alkaline conditions.

As a metal-free two-dimensional (2D) material, g-C<sub>3</sub>N<sub>4</sub> (CN) has attracted much attention in the field of photocatalytic H<sub>2</sub> evolution due to its low cost, non-toxic, metal-free, high chemical stability and easy preparation [13–16]. However, the photocatalytic activity of bulk CN is limited by the rapid recombination of photo-generated charges.

\* Corresponding authors.

E-mail addresses: [zkzheng@sdu.edu.cn](mailto:zkzheng@sdu.edu.cn) (Z. Zheng), [bbhuang@sdu.edu.cn](mailto:bbhuang@sdu.edu.cn) (B. Huang).

<https://doi.org/10.1016/j.apcatb.2022.121143>

Received 7 December 2021; Received in revised form 18 January 2022; Accepted 23 January 2022

Available online 26 January 2022

0926-3373/© 2022 Elsevier B.V. All rights reserved.

Different strategies have been employed to overcome these limitations, such as doping with noble metals (e.g. Au, Pd and Pt) as co-catalysts [17, 18], while their large-scale practical applications are limited to the scarcity and high price. In this regard, the development of noble-metal-free co-catalysts that can be applied to the large-scale plastics photoreforming is of great significance. Inspired by the excellent HER electrocatalytic activity and durability of NiMo nanoparticles in alkaline condition [19–23], NiMo nanoparticles can be used to the co-catalyst for improving the activity of PET photoreforming. However, the slow transfer of photo-excited electrons from CN to NiMo is considered to be the overall rate-limiting step for the hydrogen evolution of the photoreforming of PET.

The semiconductor interface engineering of the electron transfer layer can improve interfacial charge transfer and consequently improve photocatalytic activity [24]. Carbon nanotubes (CNTs) can be an excellent choice as co-catalyst for improving the catalytic properties due to superior chemical stability [25,26] at alkaline solution, large surface areas and superior electron mobility [27]. The coupling of CN with CNTs provides an ideal situation for improving the activity of photoreforming of plastics because CNTs can act as an excellent charge transport layer to provide an effective electron transfer network through the  $\pi$ -conjugative structure [28]. Although functionalized CNTs have been combined with CN by electrostatic interactions, CNTs can not be effectively connected to CN and perform poor effective photo-generated charge separation [29]. Poor interface contact and heterogeneity limit the photochemical activity of CN-CNTs mixtures [30,31]. Thus, it is desirable to develop a facile approach to improve the close interaction between CN and CNTs in the photoreforming of plastics system. To promote the transfer of electrons from CN to NiMo, it is an effective strategy to integrate NiMo nanoparticles and CNTs into a heterogeneous structure with CNTs as an intermediate electron transport layer.

Here, we report an in-situ derived carbon nanotubes-carbon nitride hybrids for efficient photoreforming of PET via a NiMo-assisted catalysis route (CN-CNTs-NM). The in-situ derived CN-CNTs-NM hybrids possess interconnected networks by  $\pi$ -conjugated bond. Strong  $\pi$ - $\pi$  interactions between CNTs and CN can promote electron transfer from CN to NiMo, increase carrier lifetime and improve photocatalytic activity. Moreover, CN-CNTs-NM exhibits excellent stability in PET photoreforming in alkaline environments. The hydrogen-evolution rate of CN-CNTs-NM was 14 folds higher than that of pristine CN in photoreforming of PET. In addition, terephthalate (TPA) generated during hydrolysis and photoreforming of PET can be precipitated and separated by adding acid. Furthermore, the interface  $\pi$ - $\pi$  interactions and charge transfer mechanism of CN-CNTs-NM were studied by density functional theory (DFT) calculations. Single-particle photoluminescence (PL) confirmed the charge-carrier migration pathway of CN-CNTs-NM and provided a detailed mechanism of hydrogen production from plastics.

## 2. Experimental section

### 2.1. Materials and reagents

Melamine, poly-(ethylene terephthalate) (powder, 48  $\mu\text{m}$ ), poly (lactic acid) (pellets 150  $\mu\text{m}$ ),  $\text{D}_2\text{O}$  (99.96 atom % D) and Multi-walled carbon nanotubes (MWCNTs) were obtained from Macklin. KOH, ammonium molybdate tetrahydrate were purchased from Sinopharm Chemical Reagent Co. Nickel acetate tetrahydrate were purchased from Aladdin. KOD (40 wt% in  $\text{D}_2\text{O}$ ) was purchased from Sigma-Aldrich.

### 2.2. Synthesis of CN-CNTs-NM and CN-CNTs

Synthesis of CN: CN was prepared by thermal condensation as follows [32]: the mixture of melamine and urea (weight ratio 1:2) were calcined at 500 °C for 2 h and then at 520 °C for 2 h at the heating rate of 2 °C  $\text{min}^{-1}$  in a muffle furnace.

Synthesis of CN-NiMoO<sub>x</sub>-xH<sub>2</sub>O precursor: 0.034 g (0.136 mmol)

nickel acetate tetrahydrate and 0.0147 g (0.019 mmol) ammonium molybdate tetrahydrate were added into 40 ml ultrapure water. After acetate and molybdate salt dissolved, 0.2 g as-prepared CN was added into solution with vigorous stirring for 30 min. The solution was poured into 50 ml Teflon-lined autoclave and kept at 140 °C for 5 h. The mixture was cooled down to room temperature and was vacuum filtrated with ultrapure water. The yellow solid was dried at 60 °C.

Synthesis of CN-CNTs-NM and CN-CNTs: the CN-NiMoO<sub>x</sub>-xH<sub>2</sub>O precursor was transferred into porcelain boat and calcined at 500 °C for x hours (x, equal to 0, 0.5, 1) with a heating rate of 5 °C  $\text{min}^{-1}$  in a tube furnace under flowing Ar-H<sub>2</sub> gas mixture (10% H<sub>2</sub>). As shown in Fig. S3, the samples were named CN, CN-NM and CN-CNTs-NM. The CNTs-NM was obtained at a calcination time of 2 h. To obtain CN-CNTs, the CN-CNTs-NM was dispersed into 1.0 M H<sub>2</sub>SO<sub>4</sub> with stirring for 12 h. The solid was obtained by centrifugation and drying at 80 °C. Then the solid was dispersed in 1 M H<sub>2</sub>O<sub>2</sub> and stirred for 12 h. The final product was washed by deionized water and dried at 80 °C.

### 2.3. Materials characterization

X-ray powder diffraction (XRD) patterns were conducted on Bruker AXS D8 diffractometer equipped with Cu K $\alpha$  X-ray radiation. Scanning electron microscope (SEM) and energy-dispersive X-ray spectroscopy (EDX) were performed using Hitachi S-4800. High-resolution TEM (HRTEM) images was obtained by JEOL JEM 2100 to analyze morphology and structure crystal structure information. Fourier transform infrared spectroscopy (FT-IR) was recorded on Bruker Tensor II to analyze the functional group structure of substances and the interaction between CN and CNTs. Inductively coupled plasma optical emission spectrometry (ICP-OES) measurements were completed by Agilent 5110. X-ray photoelectron spectroscopy (XPS) measurements were performed with Thermo Fisher ESCALAB XI + to analyze chemical environment of the samples. N<sub>2</sub> adsorption-desorption measurement (BET) were carried out on Builder Kubo X-1000 apparatus. The samples were degassed at 120 °C prior to the nitrogen-adsorption measurements. The multi-point BET method is used to determine the BET specific surface area within the range of relative pressure (P/P<sub>0</sub>) of 0.05–0.3. UV-vis diffuse reflectance spectroscopy (DRS) spectra were collected on Shimadzu UV-2550, with barium sulfate as a reference then in 200–800 nm wavelength range. Thermogravimetric analysis (TGA) was conducted on TGA 5500 under N<sub>2</sub> flow, from 50 °C to 1000 °C with a heating rate of 10 K  $\text{min}^{-1}$ . Raman Spectra were recorded on HORIBA Lab RAM HRE evolution with a 325 nm laser as an excitation source. Electron paramagnetic resonance (EPR) was measured on Bruker-A200. <sup>1</sup>H NMR of (AVANCE 400) to obtain the structural composition of compound.

### 2.4. Substrate pretreatment

Polymers were pretreated according to reported literature with some modifications [10]. Polymers (50 mg  $\text{ml}^{-1}$ ) were soaked in 5 M KOH in 70 °C sand bath with stirring at 450 rpm for 24 h. After cooling to room temperature, the solution was used for photoreforming of plastics.

### 2.5. Photoreforming of plastics

The 10 mg catalyst (CN, CN-NM, CN-CNTs-NM, CN-CNTs) was dispersed in 10 ml of pretreated polymer aqueous and then ultrasound for 5 min. The system was purged with Ar and connected with a cooling circulating kept at 288 K during reaction. Next, the suspension was irradiated with a 500 W Xe lamp (Simulated solar light, 95 mW  $\text{cm}^{-2}$ , Beijing, Nbet PhchemIII Photochemical Reaction Apparatus). Gas chromatography (GC, Shiweipx GC-7806) was used to collect and analyze evolved gas. The AQY was measured by similar method, applying 95 mW/ $\text{cm}^2$  LED connected to the PCX50C Discover system (Beijing Perfectlight Technology).

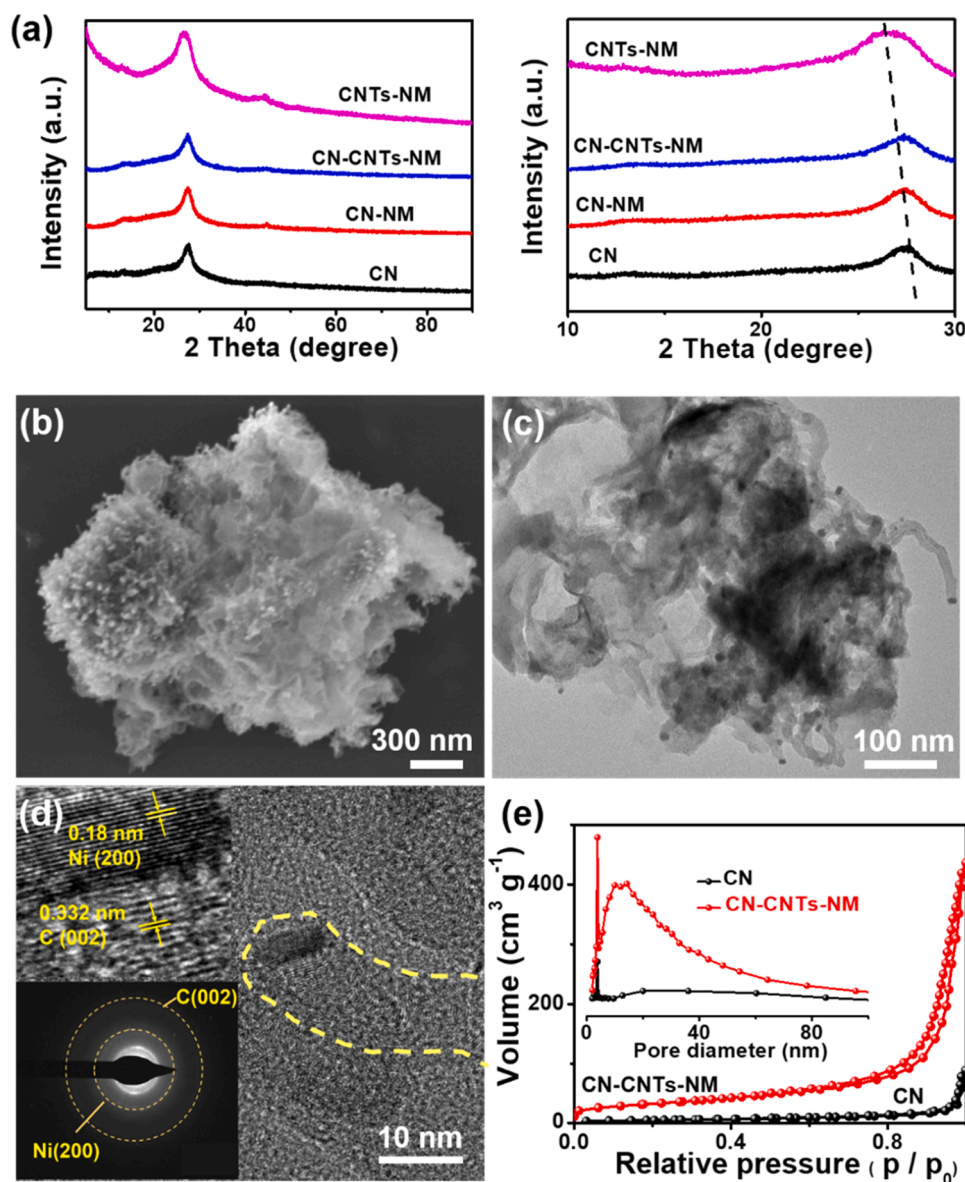


**Fig. 1.** (a) XRD patterns of CN, CN-NM, CN-CNTs-NM and CNTs-NM. (b) SEM images of CN-CNTs-NM. (c) Low magnification TEM and (d) HRTEM image and SAED pattern of CN-CNTs-NM. (e) N<sub>2</sub> adsorption-desorption isotherms of CN-CNTs-NM and CN.

### 3. Results and discussion

#### 3.1. Characterization of CN-CNTs-NM

Fig. S1 schematically illustrates the preparation process of the CN-CNTs-NM. CN, ammonium molybdate tetrahydrate and nickel acetate were used as the starting material. The mixture was hydrothermally treated to obtain CN-NiMoO<sub>x</sub>-xH<sub>2</sub>O precursor (Fig. S2). The precursor was calcined for 0.5 h at 500 °C to obtain CN-NM and CN-CNTs-NM was obtained by prolonging the heat treatment time to 1 h (Fig. S3). NiMo nanoparticles synergistically act as catalyst to derive CNTs from CN and the Ar-H<sub>2</sub> atmosphere can maintain the activity of NiMo nanoparticles catalyst to increase the amount of CNTs (Fig. S4). The structure of samples were revealed by X-ray diffraction (XRD). As shown Fig. 1a, CN and CN-CNTs-NM samples had two peaks at 27.4° and 13.0°, which were assigned to the stack of the (002) and (100) [33]. Interestingly, the intensity of diffraction peak at 26.3° corresponding to the hexagonal graphitic carbon structure [26] enhanced with the formation of CNTs. When the calcination time reached 2 h, the peak at 27.4° disappeared

and graphitic carbon became the dominant diffraction peaks, implying the transformation from the CN to CNTs. Moreover, the diffraction peak of (002) was broadened in CN-CNTs-NM hybrids compared with CN, indicating the presence of  $\pi$ - $\pi$  interaction between CN and CNTs [34]. Additionally, the weak diffraction peaks were located at 44.2° and 51.3° corresponding to (111) and (200) crystal planes of metallic Ni, respectively [35].

The scanning electron microscopy (SEM) images of CN-CNTs-NM suggested the presence of CNTs. CN had a uniform sheet-like morphology with a lateral dimension of a few microns (Fig. S5a). As shown in Fig. 1b and Fig. S5b, the in-situ derived CNTs were in the form of tube-like on the surface of CN and metal nanoparticles were well dispersed on the CNTs. In addition, it can be clearly seen from Fig. S5c that bright dots of metal nanoparticles were dispersed on CN nanosheets in CN-NM. Fig. S5d shows that the diameter of NiMo nanoparticles was about 10–15 nm, which were well dispersed on the surface of CN to form a heterojunction. The TEM image showed that CN-CNTs-NM possessed a network-like morphology composed of thin nanosheets and in-situ derived CNTs with multiple dimensions length (Fig. 1c). These results

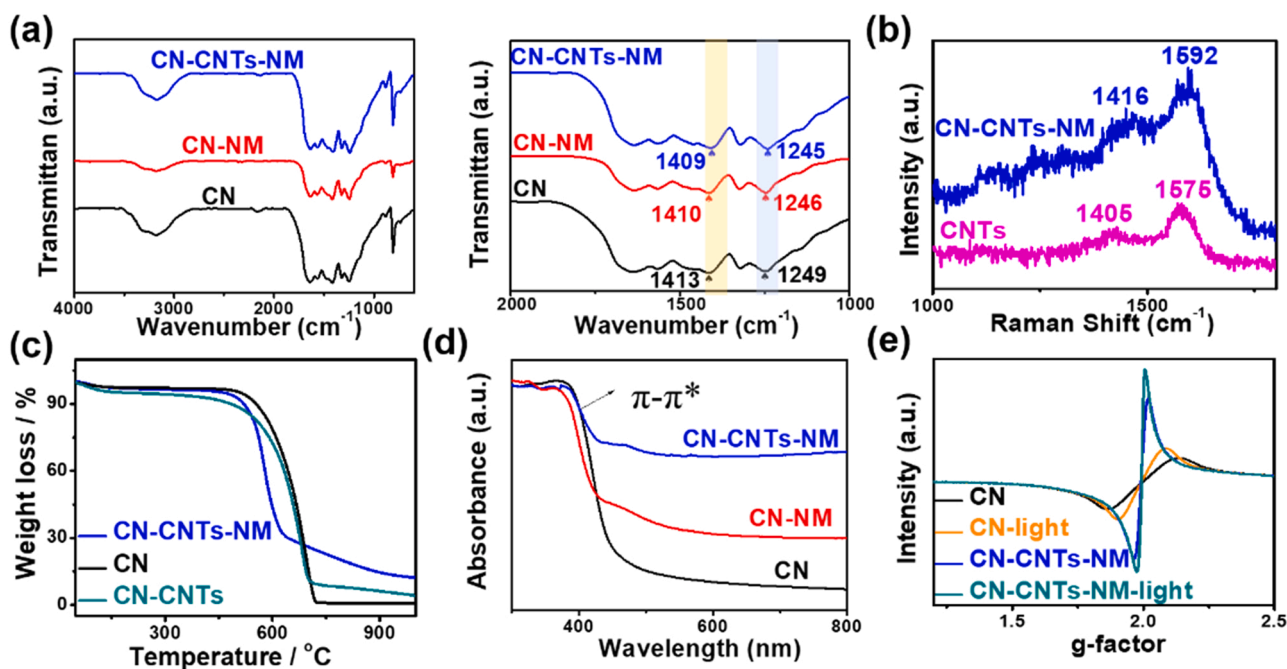


Fig. 2. (a) FTIR spectra and enlarged spectra in the range of 1000–2000  $\text{cm}^{-1}$  of CN, CN-NM and CN-CNTs-NM. (b) Raman spectra of the CNTs and CN-CNTs-NM. (c) TGA profiles of CN, CN-CNTs-NM and CN-CNTs. (d) Diffuse-reflectance spectroscopy of CN, CN-NM and CN-CNTs-NM. (e) EPR spectra of CN and CN-CNTs-NM.

indicated that CN and in situ derived CNTs have a tight interaction, which can facilitate the transfer of charge carriers. As shown in Fig. 1d, the HRTEM image shows obvious plane spacing of 0.332 nm and 0.18 nm, which correspond to the (002) plane of graphitic carbon plane [36] and (200) planes of Ni [37], respectively. As shown in Fig. 1d, the selected area diffraction pattern (SAED) reveals that the (002) plane of graphitic carbon and (200) plane of Ni nanoparticles. In addition, the weak electron diffraction ring confirmed the lower crystallinity of CN-CNTs-NM, which was consistent with the results of XRD. The STEM of CN-CNTs-NM (Fig. S5f) further verified the presence of CNTs and the distribution of NiMo nanoparticles. Meanwhile, the content of NiMo nanoparticles in CN-CNTs-NM were determined to be 6.05% by ICP-OES (Table S1). The element-mapping of CN-CNTs-NM was investigated (Fig. S6a), which was consistent with the energy-dispersive X-ray (EDX) analysis (Fig. S6b).  $\text{N}_2$  adsorption isotherm of CN-CNTs-NM (Fig. 1e) exhibited a type-IV isotherm with H3 hysteresis loop according to the IUPAC classification, which indicated the presence of mesopores structure. The Brunauer-Emmett-Teller (BET) surface area of CN-CNTs-NM was  $115.61 \text{ m}^2 \text{ g}^{-1}$  (the theoretical calculation process is shown in Fig. S7), which was approximately 7 times that of CN ( $16.87 \text{ m}^2 \text{ g}^{-1}$ ) due to the presence of the CNTs. Moreover, the pore-size of CN-CNTs-NM exhibited extra broad distribution, implying the existence of porous structure according to pore size distribution profiles. Therefore, the in situ derived CNTs can increase the surface area [38] and the porous structure can provide more active sites for photoreforming of plastics.

To confirm the formation of CNTs and the strong coupling between CN and in situ derived CNTs, the structure and chemical features of samples were studied by Fourier transform infrared spectroscopy (FTIR). The sharp peak centered at  $810 \text{ cm}^{-1}$  for all samples can be attributed to the s-triazine ring modes of CN (Fig. 2a), revealing that the structure of CN was preserved. The absorption bands at the range of  $1200\text{--}1700 \text{ cm}^{-1}$  were ascribed to the typical skeletal stretching vibrations of C-N heterocycle and the broad absorption at  $3200 \text{ cm}^{-1}$  was arising from N-H stretching vibration [39]. The C-N heterocycle stretching vibration with CN-CNTs-NM ( $1409$  and  $1245 \text{ cm}^{-1}$  respectively) exhibited shifts compared to CN ( $1413$  and  $1249 \text{ cm}^{-1}$ ), implying the strong coupling between in situ derived CNTs and CN [40]. Furthermore, the FTIR of CN-CNTs and CN confirmed the strong

coupling between in situ derived CNTs and CN (Fig. S8). To further verify the formation of CNTs and the interaction between CN and CNTs, Raman spectroscopy was used to identify the structure. As illustrated in Fig. S9, the characteristic Raman bands of CN-CNTs-NM were not different from that of CN, indicating that in situ derived CNTs had little effect on the lattice structure and molecular skeleton of CN. As shown in Fig. 2b, the Raman bands appearing at  $1400\text{--}1450 \text{ cm}^{-1}$  were assigned to D bands ( $\kappa$ -point phonons of  $A_{1g}$  symmetry) and the Raman bands appearing at  $1570\text{--}1590 \text{ cm}^{-1}$  were assigned to G bands ( $E_{2g}$  phonon of  $C \text{ sp}^2$  atoms) [41]. Remarkably, the D bands and G bands of CN-CNTs-NM were shifted compared to pure CNTs, e.g.  $1416\text{--}1405 \text{ cm}^{-1}$  and  $1592\text{--}1575 \text{ cm}^{-1}$ . The obvious shifts confirmed the electron transfer from CN to the  $\pi$  state of CNTs and the presence of the strong interaction between CN and in situ derived CNTs [42,43]. Thermogravimetric analysis (TGA) confirmed the close contact between CN and CNTs (Fig. 2c). CN began to decompose at about  $500^\circ\text{C}$ , while CN-CNTs-NM decomposed at low temperature, implying the existence of the close contact [44] between CN and in situ derived CNTs.

The optical properties of CN-CNTs-NM was determined by UV-vis diffuse reflectance spectroscopy. Fig. 2d shows that the absorption edge of CN was around  $460 \text{ nm}$  due to the  $\pi-\pi^*$  electronic transition [45]. The light absorption of CN-CNTs-NM exhibited a red shift and the  $\pi-\pi^*$  electronic transition was enhanced due to the  $\pi-\pi$  conjugated system between CN and in-situ derived CNTs. The absorption intensity of CN-CNTs-NM was enhanced due to the strong optical absorption of CNTs. In addition, it can be attributed to the fact that the in-situ derived CNTs enhanced the surface charge through  $\pi-\pi$  conjugation and promoted the electronic transition with CN [46]. The optical and electronic properties of pure CN and CN-CNTs-NM hybrid photocatalysts were examined by electron paramagnetic resonance (EPR) (Fig. 2e). Two samples exhibited one single Lorentzian line centering at a g-value of 2.0034, indicating an unpaired electron on the carbon atoms of the  $\pi$ -conjugated aromatic rings [47]. The EPR signal intensity of CN-CNTs-NM was sharper and narrower compared with CN, which is due to the fact that non-bonded  $\pi$  electrons can generate local spins at the edges of CNTs [48]. The EPR intensity of CN-CNTs-NM was enhanced compared to CN due to the well-evolved electronic structure of the  $\pi$ -conjugated system with extended delocalization and the



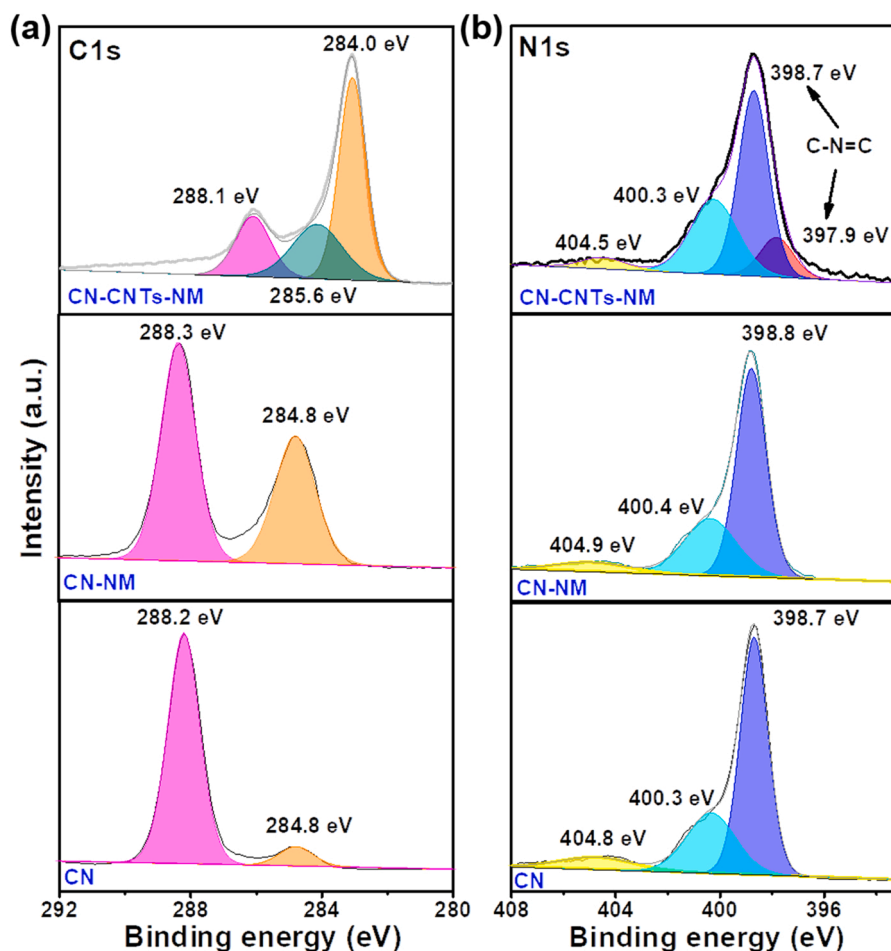


Fig. 3. XPS high-resolution spectra of (a) C1s and (b) N1s for CN, CN-NM and CN-CNTs-NM.

presence of unpaired electrons. This result indicates that CN-CNTs-NM has high carrier density and carrier separation presumably because of the  $\pi$ - $\pi$  conjugation between in-situ derived CNTs and CN. When CN and CN-CNTs-NM were illuminated, an enhanced signal for EPR was detected compared to dark. This result confirms that efficient photochemical radical pairs were generated by the  $\pi$ - $\pi$  conjugation between CN and in-situ derived CNTs, which is useful to the photocatalytic process.

The chemical composition, surface states and interface interaction were analyzed by X-ray photoelectron spectroscopy (XPS). As shown in Fig. 3a, the C 1s spectrum of CN proved the existence of  $sp^2$  C=N and C-C, which were located at 288.2 and 284.8 eV, respectively [37]. However, the C 1s spectrum of CN-CNTs-NM was different from CN. The C1s spectrum of CN-CNTs-NM could be devolved into three peaks, that is, 284.0 eV (C=C), 285.6 eV (C-OH) and 288.1 eV ( $sp^2$  carbon atoms bonded to N inside the aromatic structure) [49]. The C=C content of graphitization was increased compared with the CN, which confirmed the formation of CNTs. As shown in Fig. 3b, the N 1s spectrum of CN can be fitted with three species at binding energies of 398.7, 400.3 and 404.8 eV, which were assigned to the C-N=C, N-(C)<sub>3</sub> and  $\pi$ - $\pi^*$  excitation C-N conjugated structure [50]. As expected, the C1s and N1s of CN and CN-NM were similar. Specifically, the N 1s spectrum of CN-CNTs-NM can be fitted with four species. The peak at 398.7 eV corresponding to the  $sp^2$ -bonded N atoms in triazine rings (C-N=C) was splitted to a new shoulder peak at 397.9 eV due to the  $\pi$ - $\pi$  interaction between CN and nitrogen atoms in CNTs [51]. The Ni 2p and Mo 3d spectrum of samples were analyzed in Fig. S10. The XPS survey spectrum showed that the C content in CN-CNTs-NM was higher than CN, demonstrating the presence of CNTs (Table S2).

### 3.2. Photoreforming of plastics

The activity of photoreforming of plastics was investigated. The PET polymers were pretreated in an alkaline solution to break chemical bonds and transfer into small molecular compounds to improve photocatalytic hydrogen evolution. The  $^1\text{H}$  nuclear magnetic resonance ( $^1\text{H}$  NMR) spectrum shows that the pretreated of PET contain ethylene glycol (EG), terephthalate (TPA) and other complex small molecules (Fig. 4a). Thus, EG can act as electron donors to be oxidized in the PET photoreforming. As shown in Fig. 4a, the organic molecules after photoreforming of PET includes glyoxal and glycolate. The CN-CNTs-NM was dispersed the reaction solution for 5 min through sonication to increase activity [10]. The photoreforming of PET over CN-CNTs-NM was carried out in a pretreated solution under Ar atmosphere at 288 K (Fig. S11). Finally, TPA was precipitated by adding formic acid and separated by suction filtration to obtain white powder (Fig. 4b). The UV-VIS spectra and  $^1\text{H}$  NMR were used to detect the structure of TPA (Fig. S12). To study the effect of NiMo nanoparticles to the photoreforming of PET, the NiMo nanoparticles were removed by dispersing into 1 M  $\text{H}_2\text{SO}_4$  and 1 M  $\text{H}_2\text{O}_2$  (CN-CNTs). The content of residual NiMo nanoparticles was determined by ICP method (Table S1). The TEM images of CN-CNTs showed that NiMo nanoparticles were removed from the surface of the CN-CNTs-NM (Fig. S13a). The crystallinity and morphology of CN-CNTs were unchanged, illustrating that the CN-CNTs was stable (Fig. S13b-c). The activity of CN-CNTs was reduced compared with the CN-CNTs-NM (Fig. S13d), indicating that NiMo nanoparticles are the active sites of PET photoreforming. In the presence of CNTs, the activity was significantly enhanced, which is attributed to the strong interaction between CN and CNTs to improve interfacial carrier transfer.

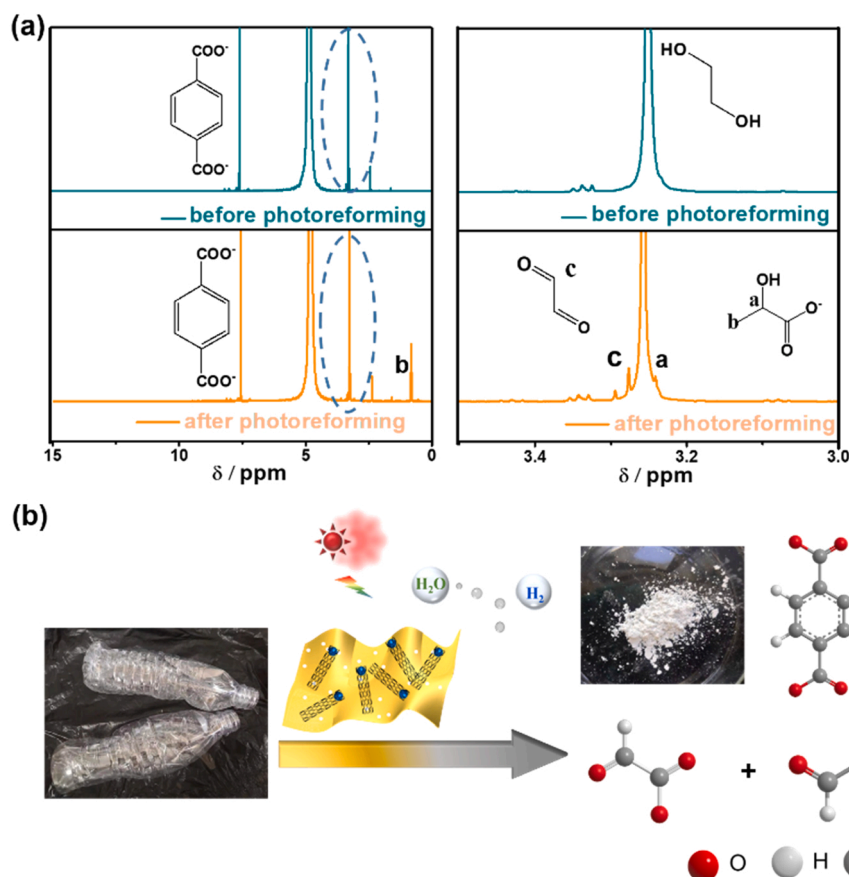


**Fig. 4.** (a)  $^1\text{H}$  NMR spectra of PET before and after photoreforming. (b) Photoreforming of PET to obtain commodity chemicals and  $\text{H}_2$  fuel. Reaction conditions: 10 ml KOH (5 M), pretreated PET (50 mg  $\text{ml}^{-1}$ ), 10 mg CN-CNTs-NM under simulated solar light for 4 h at 288 K. Light resource: simulated solar light, 95  $\text{mW cm}^{-2}$ .

No hydrogen was detected without light, substrate, catalyst or co-catalyst (Fig. 5a). This implies that light, catalyst and substrate are necessary for PET photoreforming to  $\text{H}_2$ . The photoreforming activity of different photocatalysts were evaluated. As shown in Fig. 5b, the CN-CNTs-NM exhibited the most active for photoreforming of PET, which was around 14 times higher than CN. To exclude the influence of the surface areas of the photocatalyst, the hydrogen evolution rate of the photoreforming PET was normalized to the surface area of the photocatalyst (Fig. 5c). After normalization, CN-CNTs-NM showed nearly 2 times hydrogen evolution rate higher than that of CN. Normally, alkaline conditions were required during the hydrogen evolution reaction of PET photoreforming. The highest of hydrogen evolution of PET photoreforming was  $90 \mu\text{mol g}^{-1} \text{h}^{-1}$  in 10 M KOH solution (Fig. 5d). Considering the cost of alkali and environmental pollution, 5 M KOH was selected for the pretreatment solution. Other polymers such as polylactic acid (PLA) was photoreformed under the same conditions (Fig. 5e). The hydrogen evolution of PLA was higher than that of PET. This can be attributed to the fact that the monomer of PLA is lactic acid (Fig. S14a), which is a highly efficient sacrificial agent. Formate was formed after photoreforming of PLA (Fig. S14b). The apparent quantum yield (AQY) of PET photoreforming to  $\text{H}_2$  was investigated for CN-CNTs-NM according to the previous research [52]. As shown in Fig. 5f, the AQY reached 0.56% for CN-CNTs-NM at  $420 \pm 5 \text{ nm}$ . The activity of PET photoreforming corresponds to the optical absorption spectrum (Fig. 5g), indicating that the photoreforming of PET to  $\text{H}_2$  is driven by photoinduced electrons in CN [53]. Since the activity of photocatalyst depends on the masses of the catalyst greatly, the AQY of  $\text{H}_2$  production with different mass of catalysts were studied at  $420 \pm 5 \text{ nm}$  (Fig. S15). The AQY gradually enhanced with the mass of the catalyst increasing. When the amount of catalyst was 20 mg, AQY reached the maximum

value of 0.62%.

To verify the stability of CN-CNTs-NM, the recyclability experiments of PET photoreforming were performed under the same conditions. After 4 cycles (Fig. 5h), no noticeable reduction of hydrogen evolution was observed. More importantly, the crystallinity and morphology of CN-CNTs-NM were not changed after the reaction (Fig. S16). These results suggest that the CN-CNTs-NM was stable for photoreforming of plastics, which is important to meet the requirements of actual applications. The in-situ derived CNTs can act as electron acceptors to interact well with CN due to the  $\pi$ -conjugated structure. The physical mixture of CN and CNTs showed an aggregation structure in CN-CNTs mixed (Fig. S17a), which demonstrates that the electrostatic adsorption between CN and CNTs formed poor surface contact. In addition, the hydrogen evolution over CN-CNTs mix was lower than CN-CNTs under the same conditions (Fig. S17b). The experimental results show that the in-situ derived CNTs have strong  $\pi$ - $\pi$  interactions with CN, which prolongs the lifetime of the photogenerated carrier and improves the photocatalytic activity. Furthermore, the plastic bottles were utilized for the photoreforming, demonstrating the real-world applicability of system. As shown in Fig. 5i, the hydrogen evolution rate from plastic bottles was slightly lower than that of pure PET, owing to that the plastic bottles contain various additives and long-chain polymers such as adhesives.

### 3.3. Single-particle PL measurement

To further understand the role of the in-situ derived CNTs in the photoreforming of PET, single-particle PL study were carried out. Firstly, CN and CN-CNTs-NM were well-dispersed on the quartz cover glass by spin-coating, respectively. Then single-particle PL measurement was performed with a circularly-polarized 375 nm continuous wave

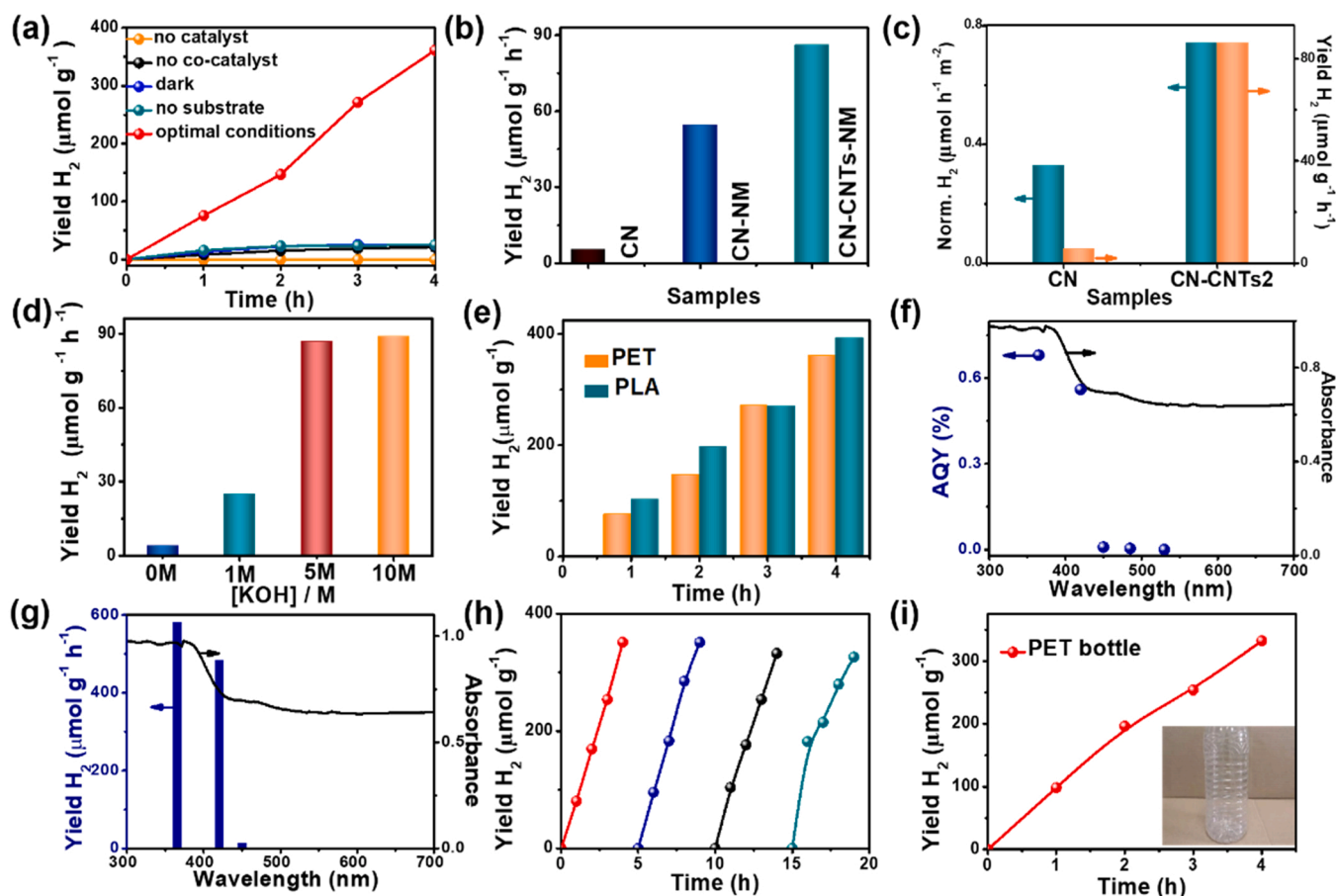


**Fig. 5.** (a) Control experiments for photoreforming of PET over CN-CNTs-NM. (b) Photoreforming of PET to  $H_2$  over prepared photocatalysts. (c) Normalized  $H_2$  evolution rate for CN and CN-CNTs-NM to specific surface area. (d) The influence of KOH concentration on photoreforming of PET to  $H_2$  using CN-CNTs-NM. (e) Photoreforming of PET and PLA over CN-CNTs-NM at the same conditions. Dependence of (f) apparent quantum yield (AQY) and (g)  $H_2$  evolution rate on different wavelength over CN-CNTs-NM (irradiated by a monochromatic LED light of  $\lambda \pm 5$  nm for 365, 420, 450, 485 and 530 nm). (h) Cycling runs of CN-CNTs-NM at the same conditions. (i) Photoreforming of PET bottle over CN-CNTs-NM. Reaction conditions unless stated otherwise in figure: 10 ml KOH (5 M), pretreated PET (50 mg ml<sup>-1</sup>), 10 mg CN-CNTs-NM under simulated solar light for 4 h at 288 K. Light resource: simulated solar light, 95 mW cm<sup>-2</sup>.

laser as the excitation source in ambient air. As shown in the PL spectra (Fig. S18), pure CN exhibited a strong emission peak at 460 nm, which was attributed to the radiative recombination of charge carriers [54]. Meanwhile, the PL images of CN-CNTs-NM exhibited an obvious quenching compared with that of CN (Fig. 6a-b). It has been reported that a higher PL intensity usually indicates faster recombination of photogenerated  $e^-$  and  $h^+$  in the semiconductor [55]. The PL intensity of CN-CNTs-NM (Fig. 6c) was quenched compared with that of CN, implying that the electron transport from CN to CNTs to NM reduced the recombination of electrons and holes. Similar results were observed from 3 individual particles of each sample (Fig. S19). Furthermore, the PL intensity of CN-CNTs was decreased compared with CN (Fig. S20), suggesting that CNTs can inhibit the recombination of photo-generated carriers through strong interface effect. In addition, the PL peaks of CN-CNTs-NM shifted to longer wavelengths, confirming the presence of strong  $\pi$ - $\pi$  conjugation between CNTs and CN. [16]. Therefore, the strong  $\pi$ - $\pi$  conjugated system of CN-CNTs-NM can promote the charge transfer process and improve the activity. The PL lifetimes decay curves were fitted by a tri-exponential decay function:  $I(t) = A_1 \exp(-t/\tau_1) + A_2 \exp(-t/\tau_2) + A_3 \exp(-t/\tau_3)$ , where  $A$  and  $\tau$  denote the amplitudes and lifetimes, respectively [54]. More importantly, it can be seen that the  $\tau_{\text{average}}$  of CN was longer than that of CN-CNTs-NM (Table S3), indicating the existence of electron transfer (ET) decay channel from CB [57]. The average lifetime of CN-CNTs-NM was decreased due to efficient electron injection from CN to NiMo through strong  $\pi$ - $\pi$  interaction between CN and in-situ derived CNTs. To further support the above

view, the transient photocurrent response of CN and CN-CNTs-NM were recorded (Fig. 6d). Obviously, the photocurrent density over CN-CNTs-NM was improved, indicating that the  $\pi$ - $\pi$  interaction between CN and in-situ derived CNTs could facilitate the separation of the photoinduced electron-hole pairs. Electrochemical impedance spectroscopy (EIS) were consistent with the photocurrent density. The arc radius of CN-CNTs-NM was the smaller than CN (Fig. 6e), indicating that the photogenerated electron-hole pairs were effectively separated and the interface charges were quickly transferred through the  $\pi$ - $\pi$  interaction.

Notably, to obtain a direct visual information, a single particle PL microscopy was used to study the hydrogen evolution reaction situ (Fig. S21). Since the release of ethylene glycol (EG) after pretreatment of PET was 60%, EG was chosen as a model molecule to explore its mechanism [11]. CN-CNTs-NM was spin-coated on the precleaned quartz cover glass with single-particle dispersion and then the cell was immersed by adding EG solution carefully. As shown in Fig. 6b, the brightness of CN-CNTs-NM was dramatically decreased after adding EG solution into the sample. Similar the PL quenching in other positions was observed when the EG was dripped into the above solution the quartz plate coated with CN-CNTs-NM (Fig. 6g and Fig. S22). The intensity change of single-particle PL fluorescence spectrum reflects the molecules chemisorbed on the surface of CN-CNTs-NM and interaction between CN-CNTs-NM and EG [58,59]. The average PL lifetime of CN-CNTs-NM immersed in EG was shorter than CN-CNTs-NM immersed in air (Fig. 6f). This phenomenon reflected the existence of

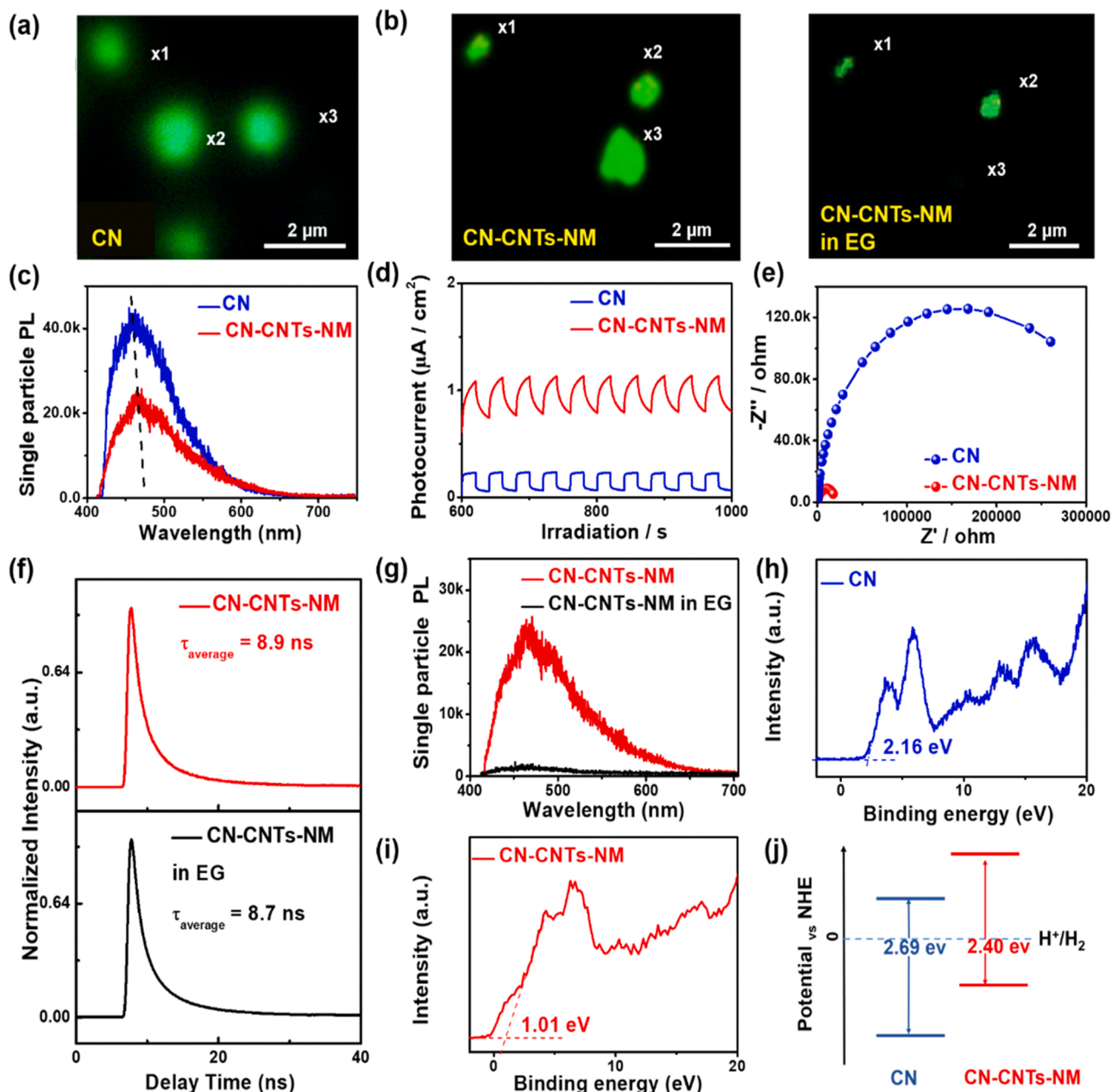


**Fig. 6.** PL image of (a) CN in air, (b) CN-CNTs-NM in air and in EG, respectively. (c) Single-particle PL spectra of CN and CN-CNTs-NM in air, respectively. (d) Transient photocurrents and (e) EIS Nyquist plots for CN and CN-CNTs-NM. (f) Single-particle time-resolved PL spectra of CN-CNTs-NM exposed to air and EG, respectively. (g) Single-particle PL spectra of CN-CNTs-NM exposed to air and EG, respectively. The VB-XPS spectra of (h) CN and (i) CN-CNTs-NM. (j) Band structure of CN and CN-CNTs-NM.

additional decay channels. Under 375 nm laser irradiation, the CN-CNTs-NM was excited and generated electron-hole pairs. The photo-generated electrons in conduction band of CN were trapped inefficiently due to the charge recombination. The in-situ derived CNTs improved the transmission efficiency of photogenerated electrons from CN to NiMo due to the existence of electron transmission channels by the  $\pi$ - $\pi$  interaction. Photo-generated electrons were injected from CN into NiMo through ET channel and then used for hydrogen proton reduction. When CN-CNTs-NM exposed in EG reaction solution, photo-generated holes were transferred to adsorbate-semiconductor interface and then oxidized the EG solution to produce ethylene glycol and glycolate.

### 3.4. Mechanism

The band structure was further optimized based on the valence band spectrum and calculated work function. To gain insight into the charge transfer behavior, the VB-XPS spectra of samples were carried out (Fig. 6h-i). Obviously, the valence band potentials of the CN-CNTs-NM exhibited negative-shift compared to CN, which reached the potential for ethylene glycol oxidation [60]. By combination of the bandgap calculated from the Kubelka-Munk plots (Fig. S23), the conduction band ( $E_{\text{CB}}$ ) of the CN and CN-CNTs-NM were calculated (Fig. 6j). A negative shift for  $E_{\text{CB}}$  level of CN-CNTs-NM was observed, which provides thermodynamic power for photoreforming of PET to produce hydrogen. Furthermore, the detailed interfacial junction and charge transfer mechanism of CN-CNTs-NM were studied by density functional theory



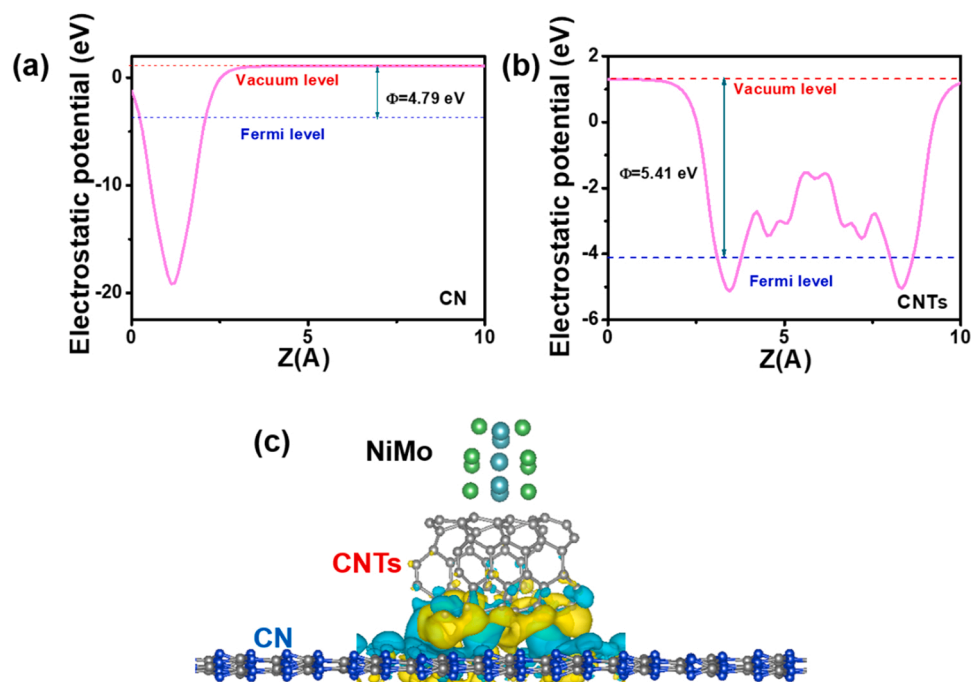


Fig. 7. Electrostatic potentials of the (a) CN and (b) CNTs. (c) Charge density difference for CN-CNTs-NM.

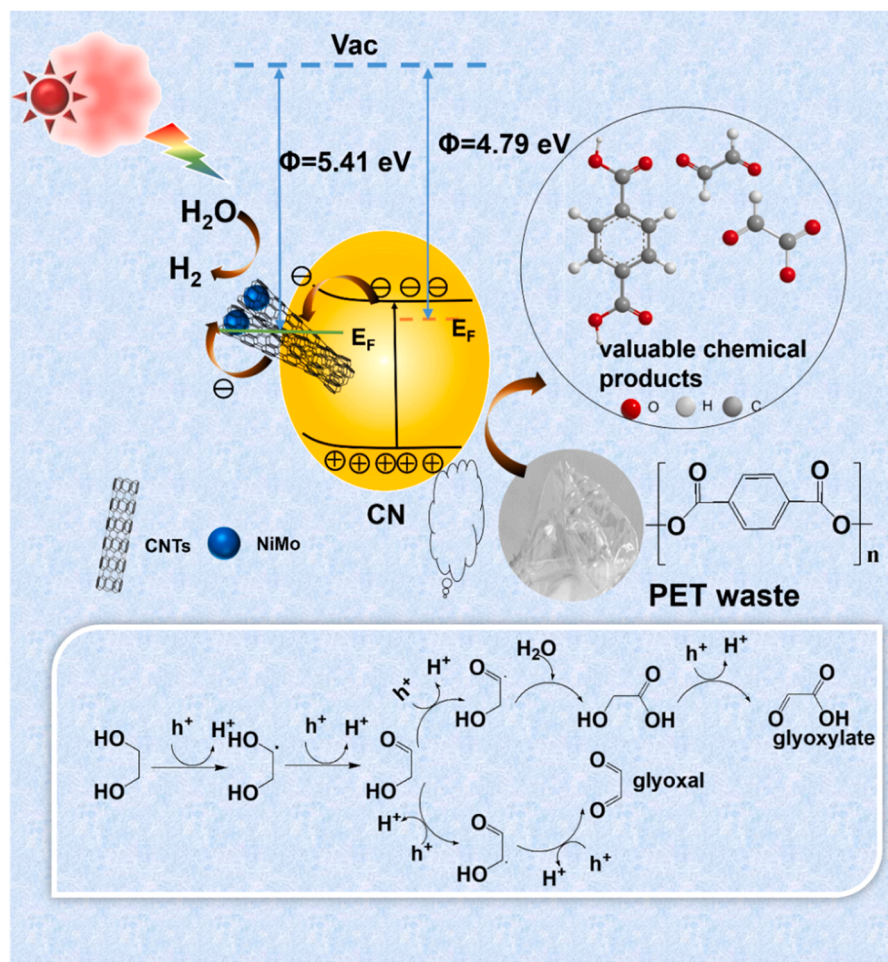


Fig. 8. Schematic diagram of the process of photoreforming of PET using CN-CNTs-NM.

(DFT) calculations. The work function for CN and CNTs were 4.79 and 5.41 eV, respectively (Fig. 7a-b), indicating that the  $E_F$  of CN was higher than that of the CNTs. When CN contacts with CNTs, electrons flow from CN to CNTs until  $E_F$  reaches thermodynamic equilibrium. Therefore, CNTs will be electron accumulation regions and CN will be electron depletion regions. Furthermore, the charge density difference of CN-CNTs-NM confirms that the electrons of CN transfer to CNTs by interfacial junction. As shown in Fig. 7c, the strong  $\pi$ - $\pi$  interaction between the in-situ derived CNTs and CN results in the redistribution of electrons. The yellow area represents electron accumulation, while the green area represents the loss of electrons. The surface of CNTs was in the state of accumulating electrons at the interface, corroborating the existence of strong electron coupling between CN and CNTs. The electron distribution at interface confirms that the delocalization of CN-CNTs was enhanced by  $\pi$ - $\pi$  interaction and promoted electron transport along the  $\pi$ - $\pi$  interaction direction.

Based on the above results, the mechanism of PET photoreforming over CN-CNTs-NM is proposed and illustrated in Fig. 8. When CN undergo photoexcitation, CN will generate photogenerated electron and hole pairs. With interfacial interaction between the CN and CNTs, the photo-excited electrons rapidly transfer from the CN to CNTs and NM. The different work functions of CNs and CNTs facilitate the separation of photo-generated electrons and holes. The  $\pi$ - $\pi$  interfacial contact between CN and CNTs can optimize the carrier behavior, reduce the transfer barrier of photocarriers and hence improve the reaction efficiency. Furthermore, in-situ derived CNTs provided electron transfer (ET) channel for photogenerated charge migration from CN to NiMo. Consequently, the photo-generated electrons interacted with hydrogen protons to generate hydrogen. The photo-generated holes can oxidize the organics in the plastic to form glyoxal and carboxylate [11], which was confirmed by monitoring the EG oxidation reactions at the single nanoparticle level.

#### 4. Conclusion

In summary, we have successfully developed in-situ derived CNTs hybridized on CN via a NiMo-assisted catalysis route as a highly efficient and stable photocatalyst for photoreforming of plastics. The  $\pi$ - $\pi$  interaction between the in-situ derived CNTs and CN facilitates charge separation and rapid carrier transfer by CNTs as an intermediate electron transport layer, which provides a simple method for designing intimate and effective interfacial junctions for photocatalytic application. CN-CNTs-NM exhibited remarkably  $H_2$  production in plastics photoreforming, which was 14 times higher than CN. This work provides direct evidence for the strong interaction between CN-CNTs-NM and EG via monitoring the single-particle PL spectra, which is important to explain the mechanism of photoreforming of plastics. CN-CNTs-NM takes advantage of abundant and freely available plastic waste to generate  $H_2$  and valuable chemicals. Hence, photoreforming of plastics is a technology that can simultaneously solve the global challenges of plastic pollution and renewable hydrogen.

#### Author contribution

Xueqin Gong. designed, preformed the experiments and wrote the paper. Fengxia Tong, Fahao Ma, Yujia Zhang and Peng Zhou. analyzed the data and discussed the manuscript. Zeyan Wang, Peng Wang, Yuan-yuan Liu, Hefeng Cheng and Ying Dai. supervised the research. Zhaoke Zheng and Baibiao Huang. conceived and initiated the research.

#### Declaration of Competing Interest

The authors declare that they have no known competing financial interests or personal relationships that could have appeared to influence the work reported in this paper.

#### Acknowledgements

This work was financially supported by the National Key Research and Development Program of China (2020YFA0710301), National Natural Science Foundation of China (No. 22072072, 51972195, 21832005 and 21972078), Natural Science Foundation of Shandong Province (ZR2019QB005, ZR2021JQ06), Shandong University Multi-disciplinary Research and Innovation Team of Young Scholars (2020QNQT11, 2020QNQT012), Qilu Young Scholars and Outstanding Young Scholars Projects of Shandong University, Taishan Scholar Foundation of Shandong Province.

#### Appendix A. Supporting information

Supplementary data associated with this article can be found in the online version at doi:10.1016/j.apcatb.2022.121143.

#### References

- [1] F. Zhang, M. Zeng, R.D. Yappert, J. Sun, Y. Lee, A.M. LaPointe, B. Peters, M. Abu-Omar, S.L. Scott, Polyethylene upcycling to long-chain alkylaromatics by tandem hydrogenolysis/aromatization, *Science* 3 (2020) 437–441, <https://doi.org/10.1126/science.abc5441>.
- [2] V. Tournier, C.M. Topham, A. Gilles, B. David, C. Folgoas, E. Moya-Leclair, E. Kamionka, M. Cot, E. Guémar, M. Dalibey, J. Nomme, G. Cioci, S. Barbe, M. Chateau, I. André, S. Duquesne, A. Marty, An engineered PET depolymerase to break down and recycle plastic bottles, *Nature* 580 (2020) 216–219, <https://doi.org/10.1038/s41586-020-2149-4>.
- [3] E. MacArthur, Beyond plastic waste, *Science* 358 (2017) 843, <https://doi.org/10.1126/science.aao6749>.
- [4] D.H. Kim, D.O. Han, K.I. Shim, J.K. Kim, J.G. Pelton, M.H. Ryu, J.C. Joo, J.W. Han, H.T. Kim, K.H. Kim, One-Pot chemo-bioprocess of PET depolymerization and recycling enabled by a biocompatible catalyst, *betaine*, *ACS Catal.* 11 (2021) 3996–4008, <https://doi.org/10.1021/acscatal.0c04014>.
- [5] X. Jiao, K. Zheng, Z. Hu, S. Zhu, Y. Sun, Y. Xie, Conversion of waste plastics into value-added carbonaceous fuels under mild conditions, *Adv. Mater.* 33 (2021), 2005192, <https://doi.org/10.1002/adma.202005192>.
- [6] S. Wageh, A.A. Al-Ghamdi, R. Jafer, X. Li, P. Zhang, A new heterojunction in photocatalysis: S-scheme heterojunction, *Chin. J. Catal.* 42 (2021) 667–669, [https://doi.org/10.1016/S1872-2067\(20\)63705-6](https://doi.org/10.1016/S1872-2067(20)63705-6).
- [7] Y.J. Zhang, Z.F. Xu, G.Y. Li, X.J. Huang, W.C. Hao, Y.P. Bi, Direct observation of oxygen vacancy self-healing on  $TiO_2$  photocatalysts for solar water splitting, *Angew. Chem. Int. Ed.* 58 (2019) 14229–14233, <https://doi.org/10.1002/ange.201907954>.
- [8] C.H. Han, L.L. Du, M. Konarova, D.C. Qi, D.L. Phillips, J.S. Xu, Beyond hydrogen evolution: solar-driven, water-donating transfer hydrogenation over platinum/carbon nitride, *ACS Catal.* 10 (2020) 9227–9235, <https://doi.org/10.1021/acscatal.0c01932>.
- [9] X. Zong, H. Yan, G. Wu, G. Ma, F. Wen, L. Wang, C. Li, Enhancement of photocatalytic  $H_2$  evolution on CdS by loading  $MoS_2$  as cocatalyst under visible light irradiation, *J. Am. Chem. Soc.* 130 (2008) 7176–7177, <https://doi.org/10.1021/ja8007825>.
- [10] T. Uekert, M.F. Kuehnle, D.W. Wakerley, E. Reisner, Plastic waste as a feedstock for solar-driven  $H_2$  generation, *Energy Environ. Sci.* 11 (2018) 2853–2857, <https://doi.org/10.1039/c8ee01408f>.
- [11] T. Uekert, H. Kasap, E. Reisner, Photoreforming of nonrecyclable plastic waste over a carbon nitride/nickel phosphide catalyst, *J. Am. Chem. Soc.* 141 (38) (2019) 15201–15210, <https://doi.org/10.1021/jacs.9b06872>.
- [12] T. Kawai, T. Sakata, Photocatalytic hydrogen production from water by the decomposition of poly-vinylchloride, protein, algae, dead insects, and excrement, *Chem. Lett.* 10 (1981) 81–84, <https://doi.org/10.1246/cl.1981.81>.
- [13] J.S. Xu, M. Antonietti, Beyond hydrogen evolution: solar-driven, water donating transfer hydrogenation over platinum/carbon nitride, *J. Am. Chem. Soc.* 139 (2017) 6026–6029, <https://doi.org/10.1021/jacs.6b11346>.
- [14] R.C. Shen, K.L. He, A.P. Zhang, N. Li, Y.H. Ng, P. Zhang, J. Hu, X. Li, In-situ construction of metallic  $Ni_3C@Ni$  core-shell cocatalysts over g- $C_3N_4$  nanosheets for shell-thickness-dependent photocatalytic  $H_2$  production, *Appl. Catal. B Environ.* 291 (2021), 120104, <https://doi.org/10.1016/j.apcatb.2021.120104>.
- [15] G.G. Zhang, M. Liu, T. Heil, S. Zafeirotas, A. Savateev, M. Antonietti, X.C. Wang, Optimizing optical absorption, exciton dissociation, and charge transfer of a polymeric carbon nitride with ultrahigh solar hydrogen production activity, *Angew. Chem. Int. Ed.* 56 (2017) 14950–14954, <https://doi.org/10.1002/ange.201706870>.
- [16] J.S. Zhang, G.G. Zhang, X.F. Chen, S. Lin, L. Mchlmann, G.D.G. Lipner, M. Antonietti, S. Blechert, X.C. Wang, Co-Monomer control of carbon nitride semiconductors to optimize hydrogen evolution with visible light, *Angew. Chem. Int. Ed.* 51 (2012) 3183–3187, <https://doi.org/10.1002/anie.201106656>.
- [17] J.S. Cai, J.Y. Huang, S.C. Wang, J. Iocozzia, Z.T. Sun, J.Y. Sun, Y.K. Yang, Y.K. Lai, Z.Q. Lin, Crafting mussel-inspired metal nanoparticle-decorated ultrathin graphitic carbon nitride for the degradation of chemical pollutants and production of

- chemical resources, *Adv. Mater.* 31 (2019), 1806314, <https://doi.org/10.1002/adma.201806314>.
- [18] K. Gu, X. Pan, W. Wang, J. Ma, Y. Sun, H. Yang, H. Shen, Z. Huang, H. Liu, In situ growth of Pd nanosheets on g-C<sub>3</sub>N<sub>4</sub> nanosheets with well-contacted interface and enhanced catalytic performance for 4-nitrophenol reduction, *Small* 14 (2018), 1801812, <https://doi.org/10.1002/smll.201801812>.
- [19] L.J. Yang, L.L. Zeng, H. Liu, Y.Q. Deng, Z.Q. Zhou, J.Y. Yu, H. Liu, W.J. Zhou, Hierarchical microsphere of MoNi porous nanosheets as electrocatalyst and cocatalyst for hydrogen evolution reaction, *Appl. Catal. B Environ.* 249 (2019) 98–105, <https://doi.org/10.1016/j.apcatb.2019.02.062>.
- [20] Q. Zhang, W. Xiao, W.H. Guo, Y.X. Yang, J.L. Lei, H.Q. Luo, N.B. Li, Macroporous array induced multiscale modulation at the surface/interface of Co(OH)<sub>2</sub>/NiMo self-supporting electrode for effective overall water splitting, *Adv. Funct. Mater.* 31 (2021), 2102117, <https://doi.org/10.1002/adfm.202102117>.
- [21] Y.-Y. Chen, Y. Zhang, X. Zhang, T. Tang, H. Luo, S. Niu, Z.-H. Dai, L.-J. Wan, J.-S. Hu, Self-templated fabrication of MoNi<sub>4</sub>/MoO<sub>3-x</sub> nanorod arrays with dual active components for highly efficient hydrogen evolution, *Adv. Mater.* 29 (2017), 1703311, <https://doi.org/10.1002/adma.201703311>.
- [22] W. Liu, Y.S. Yang, L.F. Chen, E.Z. Xu, J.M. Xu, S. Hong, X. Zhang, M. Wei, Atomically-ordered active sites in NiMo intermetallic compound toward low-pressure hydrodeoxygenation of furfural, *Appl. Catal. B Environ.* 282 (2021), 119569, <https://doi.org/10.1016/j.apcatb.2020.119569>.
- [23] K.A. Worsley, I. Kalinin, E. Bekyarova, R.C. Haddon, Functionalization and dissolution of nitric acid treated single-walled carbon nanotubes, *J. Am. Chem. Soc.* 131 (50) (2009) 18153–18158, <https://doi.org/10.1021/ja906267g>.
- [24] H. Kasap, R. Godin, C. Jeay-Bizot, D.S. Achilleos, X. Fang, J.R. Durrant, E. Reisner, Interfacial engineering of a carbon nitride-graphene oxide-molecular Ni catalyst hybrid for enhanced photocatalytic activity, *ACS Catal.* 8 (2018) 6914–6926, <https://doi.org/10.1021/acscatal.8b01969>.
- [25] L. Cheng, H.W. Zhang, X. Li, J.J. Fan, Q.J. Xiang, Carbon-graphitic carbon nitride hybrids for heterogeneous photocatalysis, *Small* (2020), 2005231, <https://doi.org/10.1002/smll.202005231>.
- [26] X. Liu, W. Yang, L. Chen, Z. Liu, L. Long, S. Wang, C. Liu, S. Dong, J. Jia, Graphitic carbon nitride (g-C<sub>3</sub>N<sub>4</sub>)-derived bamboo-like carbon nanotubes/Co nanoparticles hybrids for highly efficient electrocatalytic oxygen reduction, *ACS Appl. Mater. Interfaces* 12 (2020) 4463–4472, <https://doi.org/10.1021/acsami.9b18454>.
- [27] Y.M. Zhong, J.L. Yuan, J.Q. Wen, X. Li, Y.H. Xu, W. Liu, S.S. Zhang, Y.P. Fang, Earth-abundant NiS co-catalyst modified metal-free mpg-C<sub>3</sub>N<sub>4</sub>/CNT nanocomposites for highly efficient visible-light photocatalytic H<sub>2</sub> evolution, *Dalton Trans.* 44 (2015), <https://doi.org/10.1039/c5dt02693h>.
- [28] L. Ge, C.C. Han, Synthesis of MWNTs/g-C<sub>3</sub>N<sub>4</sub> Composite photocatalysts with efficient visible light photocatalytic hydrogen evolution activity, *Appl. Catal. B Environ.* 117–118 (2012) 268–274, <https://doi.org/10.1016/j.apcatb.2012.01.021>.
- [29] Y. Zhao, F. Zhao, X. Wang, C. Xu, Z. Zhang, G. Shi, L. Qu, Graphitic carbon nitride nanoribbons: graphene-assisted formation and synergic function for highly efficient hydrogen evolution, *Angew. Chem. Int. Ed.* 53 (2014) 13934–13939, <https://doi.org/10.1002/anie.201403946>.
- [30] J. Li, D. Wu, J. Iocozzia, H. Du, X. Liu, Y. Yuan, W. Zhou, Achieving efficient incorporation of  $\pi$ -electrons into graphitic carbon nitride for markedly improved hydrogen generation, *Angew. Chem. Int. Ed.* 58 (2019) 1985–1989, <https://doi.org/10.1002/anie.201813117>.
- [31] C. Xu, X. Liu, D. Li, Z. Chen, J. Yang, J. Huang, H. Pan, Coordination of  $\pi$ -delocalization in g-C<sub>3</sub>N<sub>4</sub> for efficient photocatalytic hydrogen evolution under visible light, *ACS Appl. Mater. Interfaces* 13 (2021) 20114–20124, <https://doi.org/10.1021/acsaami.1c02722>.
- [32] D.M. Ruan, S. Kim, M. Fujitsuka, T. Majima, Defects rich g-C<sub>3</sub>N<sub>4</sub> with mesoporous structure for efficient photocatalytic H<sub>2</sub> production under visible light irradiation, *Appl. Catal. B Environ.* 238 (2018) 638–646, <https://doi.org/10.1016/j.apcatb.2018.07.028>.
- [33] Y.T. Xiao, G.H. Tian, W. Li, Y. Xie, B.J. Jiang, C.G. Tian, D.Y. Zhao, H.G. Fu, Molecule self-assembly synthesis of porous few-layer carbon nitride for highly efficient photoredox catalysis, *J. Am. Chem. Soc.* 141 (2019) 2508–2515, <https://doi.org/10.1021/jacs.8b12428>.
- [34] J. Xu, Q.Z. Gao, Z.P. Wang, Y.F. Zhu, An all-organic 0D/2D supramolecular porphyrin/g-C<sub>3</sub>N<sub>4</sub> heterojunction assembled via  $\pi$ - $\pi$  interaction for efficient visible photocatalytic oxidation, *Appl. Catal. B Environ.* 291 (2021), 120059, <https://doi.org/10.1016/j.apcatb.2021.120059>.
- [35] J. Zhang, T. Wang, P. Liu, Z.Q. Liao, S.H. Liu, X.D. Zhuang, M.W. Chen, E. Zschech, X.L. Feng, Efficient hydrogen production on MoNi<sub>4</sub> electrocatalysts with fast water dissociation kinetics, *Nat. Commun.* 8 (2017) 15473, <https://doi.org/10.1038/ncomms15437>.
- [36] Q.X. Liu, C.M. Zeng, Z.H. Xie, L.H. Ai, Y.Y. Liu, Q. Zhou, J. Jiang, H.Q. Sun, S. B. Wang, Cobalt @ nitrogen-doped bamboo-structured carbon nanotube to boost photocatalytic hydrogen evolution on carbon nitride, *Appl. Catal. B Environ.* 254 (2019) 443–451, <https://doi.org/10.1016/j.apcatb.2019.04.098>.
- [37] X. Han, D.Y. Xu, L. An, C.Y. Hou, Y.G. Li, Q.H. Zhang, H.Z. Wang, Ni-Mo nanoparticles as co-catalyst for drastically enhanced photocatalytic hydrogen production activity over g-C<sub>3</sub>N<sub>4</sub>, *Appl. Catal. B Environ.* 243 (2018) 136–144, <https://doi.org/10.1016/j.apcatb.2018.10.003>.
- [38] Q. Han, B. Wang, J. Gao, L.T. Qu, Graphitic carbon nitride/nitrogen-rich carbon nanofibers: highly efficient photocatalytic hydrogen evolution without cocatalysts, *Angew. Chem. Int. Ed.* 127 (2015) 11595–11599, <https://doi.org/10.1002/anie.201605591>.
- [39] D.J. Martin, K.P. Qiu, S.A. Shevlin, A.D. Handoko, X.W. Chen, Z.X. Guo, J.W. Tang, Highly efficient photocatalytic H<sub>2</sub> evolution from water using visible light and structure-controlled graphitic carbon nitride, *Angew. Chem. Int. Ed.* 126 (2014) 9394–9399, <https://doi.org/10.1002/ange.201403375>.
- [40] Y.G. Wang, Q.N. Xia, X. Bai, Z.G. Ge, Q. Yang, C.C. Yin, S.F. Kang, M.D. Dongd, X. Li, Carbothermal activation synthesis of 3D porous g-C<sub>3</sub>N<sub>4</sub>/carbon nanosheets composite with superior performance for CO<sub>2</sub> photoreduction, *Appl. Catal. B Environ.* 239 (2018) 196–203, <https://doi.org/10.1016/j.apcatb.2018.08.018>.
- [41] A.M. Rao, P.C. Eklund, S. Bandow, A. Thess, R.E. Smalley, Evidence for charge transfer in doped carbon nanotube bundles from Raman scattering, *Nature* 388 (1997) 257–259, <https://doi.org/10.1038/40827>.
- [42] Y.L. Chen, J.H. Li, Z.H. Hong, B. Shen, B.Z. Lin, B.F. Gao, Origin of the enhanced visible-light photocatalytic activity of CNT modified g-C<sub>3</sub>N<sub>4</sub> for H<sub>2</sub> production, *Phys. Chem. Chem. Phys.* 16 (2014) 8106–8113, <https://doi.org/10.1039/c3cp55191a>.
- [43] R. Kitaura, N. Imazu, K. Kobayashi, H. Shinohara, Fabrication of metal nanowires in carbon nanotubes via versatile nano-template reaction, *Nano Lett.* 8 (2008) 693–699, <https://doi.org/10.1021/nl073070d>.
- [44] K.C. Christoforidis, Z. Syrgiannis, V.L. Parola, T. Montini, C. Petit, E. Stathatos, R. Godin, J.R. Durrant, M. Prato, P. Fornasiero, Metal-free dual-phase full organic carbon nanotubes/g-C<sub>3</sub>N<sub>4</sub> heteroarchitectures for photocatalytic hydrogen production, *Nano Energy* 50 (2018) 468–478, <https://doi.org/10.1016/j.nanoen.2018.05.070>.
- [45] S.F. An, G.H. Zhang, K.Y. Li, Z.N. Huang, X. Wang, Y.K. Guo, J.G. Hou, C.S. Song, X. W. Guo, Self-supporting 3D carbon nitride with tunable  $n \rightarrow \pi^*$  electronic transition for enhanced solar hydrogen production, *Adv. Mater.* (2021), 2104361, <https://doi.org/10.1002/adma.202104361>.
- [46] S. Zhao, T. Guo, X. Lia, T.G. Xue, B. Yang, X. Zhao, Carbon nanotubes covalent combined with graphitic carbon nitride for photocatalytic hydrogen peroxide production under visible light, *Appl. Catal. B Environ.* 224 (2018) 725–732, <https://doi.org/10.1016/j.apcatb.2017.11.005>.
- [47] G.S. Li, Z.P. Xie, S.M. Chai, X. Chen, X.C. Wang, A facile one-step fabrication of holey carbon nitride nanosheets for visible-light-driven hydrogen evolution, *Appl. Catal. B Environ.* 283 (2021), 119637, <https://doi.org/10.1016/j.apcatb.2020.119637>.
- [48] P. Karthik, R. Vinoth, P. Zhang, W. Choi, E. Balaraman, B. Neppolian,  $\pi$ - $\pi$  interaction between metal-organic framework and reduced graphene oxide for visible-light photocatalytic H<sub>2</sub> production, *ACS Appl. Energy Mater.* 1 (2018) 1913–1923, <https://doi.org/10.1021/acsaem.7b00245>.
- [49] S.M. Miranda, G.E. Romanos, V. Likodimos, R.R.N. Marques, E.P. Favvas, F. K. Katsaros, K.L. Stefanopoulos, V.J.P. Vilar, J.L. Fariaa, P. Falaras, A.M.T. Silva, Pore structure, interface properties and photocatalytic efficiency of hydration/dehydration derived TiO<sub>2</sub>/CNT composites, *Appl. Catal. B Environ.* 147 (2014) 65–81, <https://doi.org/10.1016/j.apcatb.2013.08.013>.
- [50] X.P. Han, W. Zhang, X.Y. Ma, C. Zhong, N.Q. Zhao, W.B. Hu, Y.D. Deng, Identifying the activation of bimetallic sites in NiCo<sub>2</sub>S<sub>4</sub>@g-C<sub>3</sub>N<sub>4</sub>-CNT hybrid electrocatalysts for synergistic oxygen reduction and evolution, *Adv. Mater.* 31 (2019), 1808281, <https://doi.org/10.1002/adma.201808281>.
- [51] E.J. Son, S.H. Lee, S.K. Kuk, M. Pesic, D.S. Choi, J.W. Ko, K. Kim, F. Hollmann, C. B. Park, Carbon nanotube graphitic carbon nitride hybrid films for flavoenzyme-catalyzed photoelectrochemical cells, *Adv. Funct. Mater.* 28 (2018), 1705232, <https://doi.org/10.1002/adfm.201705232>.
- [52] G.G. Zhang, M.W. Zhang, X.X. Ye, X.Q. Qiu, S. Lin, X.C. Wang, Iodine modified carbon nitride semiconductors as visible light photocatalysts for hydrogen evolution, *Adv. Mater.* 26 (2014) 805–809, <https://doi.org/10.1002/adma.201303611>.
- [53] Q. Han, B. Wang, J. Gao, Z.H. Cheng, Y. Zhao, Z.P. Zhang, L.T. Qu, Atomically thin mesoporous nanomesh of graphitic C<sub>3</sub>N<sub>4</sub> for high-efficiency photocatalytic hydrogen evolution, *ACS Nano* 10 (2) (2016) 2745–2751, <https://doi.org/10.1021/acsnano.5b07831>.
- [54] W.-J. Ong, L.K. Putri, Y.-C. Tan, L.-L. Tan, N. Li, Y.H. Ng, X.M. Wen, S.-P. Cha, Unravelling charge carrier dynamics in protonated g-C<sub>3</sub>N<sub>4</sub> interfaced with carbon nanodots as co-catalysts toward enhanced photocatalytic CO<sub>2</sub> reduction: a combined experimental and first-principles DFT study, *Nano Res.* 10 (2017) 1673–1696, <https://doi.org/10.1007/s12274-016-1391-4>.
- [55] Y.L. Lia, X.F. Xu, J.S. Wang, W. Luo, Z.P. Zhang, X. Cheng, J.S. Wu, Y.L. Yang, G. Chen, S.R. Sun, L.Z. Wang, Post-redox engineering electron configurations of atomic thick C<sub>3</sub>N<sub>4</sub> nanosheets for enhanced photocatalytic hydrogen evolution, *Appl. Catal. B Environ.* 270 (2020), 118855, <https://doi.org/10.1016/j.apcatb.2020.118855>.
- [57] J.W. Xue, M. Fujitsuka, T. Majima, Shallow rap state-induced efficient electron transfer at the interface of heterojunction photocatalysts: the crucial role of vacancy defects, *ACS Appl. Mater. Interfaces* 11 (2019) 40860–40867, <https://doi.org/10.1021/acsaami.9b14128>.
- [58] F.X. Tong, X.Z. Liang, F.H. Ma, X.L. Bao, Z.Y. Wang, Y.Y. Liu, P. Wang, H.F. Cheng, Y. Dai, B.B. Huang, Z.K. Zheng, Plasmon-mediated nitrobenzene hydrogenation with formate as the hydrogen donor studied at a single-particle level, *ACS Catal.* 11 (2021) 3801–3809, <https://doi.org/10.1021/acscatal.1c00164>.
- [59] Z.K. Zheng, T. Tachikawa, T. Majima, Plasmon-enhanced formic acid dehydrogenation using anisotropic Pd-Au nanorods studied at the single-particle level, *J. Am. Chem. Soc.* 137 (2015) 948–957, <https://doi.org/10.1021/ja511719g>.
- [60] H. Zhou, Y. Ren, Z.H. Li, M. Xu, Y. Wang, R.X. Ge, X.G. Kong, L.R. Zheng, H. H. Duan, Electrocatalytic upcycling of polyethylene terephthalate to commodity chemicals and H<sub>2</sub> fuel, *Nat. Commun.* 12 (2021) 4679, <https://doi.org/10.1038/s41467-021-25048-x>.